

Quasi-deterministic Localization of Er Emitters in Thin Film TiO₂ through Submicron-scale Crystalline Phase Control

Sean E. Sullivan,^{1, a)} Jonghoon Ahn,^{2,3, a)} Tao Zhou,⁴ Preetha Saha,¹ Martin V. Holt,⁴ Supratik Guha,^{5,3} F. J. Heremans,^{2,3,5} and Manish Kumar Singh¹

¹⁾*memQ, Inc. Chicago, IL 60615, United States*

²⁾*Center for Molecular Engineering, Argonne National Laboratory, Lemont, IL 60439, United States*

³⁾*Materials Science Division, Argonne National Laboratory, Lemont, IL 60439, United States*

⁴⁾*Center for Nanoscale Materials, Argonne National Laboratory, Lemont, IL 60439, United States*

⁵⁾*Pritzker School of Molecular Engineering, University of Chicago, Chicago, IL 60637, United States*

(Dated: 30 August 2023)

With their shielded 4f orbitals, rare-earth ions (REIs) offer optical and electron spin transitions with good coherence properties even when embedded in a host crystal matrix, highlighting their utility as promising quantum emitters and memories for quantum information processing. Among REIs, trivalent erbium (Er³⁺) uniquely has an optical transition in the telecom C-band, ideal for transmission over optical fibers, and making it well-suited for applications in quantum communication. The deployment of Er³⁺ emitters into a thin film TiO₂ platform has been a promising step towards scalable integration; however, like many solid-state laser systems, the deterministic spatial placement of quantum emitters remains an open challenge. We investigate laser annealing as a means to locally tune the optical resonance of Er³⁺ emitters in TiO₂ thin films on Si. Using both nanoscale X-ray diffraction measurements and cryogenic photoluminescence spectroscopy, we show that tightly focused below-gap laser annealing can induce anatase to rutile phase transitions in a nearly diffraction-limited area of the films and improve local crystallinity through grain growth. As a percentage of the Er:TiO₂ is converted to rutile, the Er³⁺ optical transition blueshifts by 13 nm. We explore the effects of changing laser annealing time and show that the amount of optically active Er:rutile increases linearly with laser power. We additionally demonstrate local phase conversion on microfabricated Si structures, which holds significance for quantum photonics.

I. INTRODUCTION

Solid-state quantum emitters in wide-bandgap semiconductors offer atom-like level structures, making them candidate optically addressable spin qubits.¹ Among these quantum emitters, rare-earth ions (REIs), are promising for applications in quantum information processing owing to their long optical² and spin coherence times.^{3–5} Trivalent erbium (Er³⁺), in particular, offers an optical transition in the telecom C-band (near 1.5 μm), which is well suited for optical fiber-based quantum communication.⁶ In addition, integration of Er-doped crystals with nanophotonic cavities has enabled emission of both single⁷ and indistinguishable⁸ photons, and single-shot optical readout of hyperfine spin states.^{9,10} In contrast to trapped neutral atoms or ions, the properties of solid-state spin qubits are intimately tied to their environment, i.e., the host crystal in which they are embedded. While the local crystal environment can be a source of noise or relaxation from charge carriers or phonons, it also offers a potential phase space for tuning the properties of the quantum emitter through materi-

als engineering. Although the 4f-4f optical transitions of REIs are somewhat shielded from nearby sources of noise, the optical lifetimes, optical coherence, and transition energies are nevertheless influenced by the local crystal environment.¹¹ For Er³⁺, several suitable oxide host materials have been identified that minimize the REIs first-order sensitivity to local electric fields by virtue of inversion-symmetric crystal sites.¹² Furthermore, the spin coherence properties of these REIs can be enhanced by selecting host crystals with a naturally low abundance of isotopes that have nuclear spins, which can introduce phase noise through magnetic dipolar interactions.^{4,13,14} One such promising host material on both accounts is TiO₂, which has been explored as a host material with very low inhomogeneous broadening (< 460 MHz) in its bulk crystalline form.¹⁵

Importantly, high quality TiO₂ films can readily be synthesized and integrated into standard CMOS process flows,¹⁶ enabling a pathway towards scalable fabrication. Given its standard thin film integration, several recent works have investigated TiO₂ thin films as a host for Er quantum emitters in rutile, anatase, and mixed-phase polycrystalline forms.^{17–19} These works showed that optical properties of the TiO₂ films could be tuned through engineering of the thin film stack by delta doping, epitaxial growth, or by adjusting the growth temperature to

^{a)}These authors contributed equally.; Electronic mail: sean@memq.tech

select either the lower temperature anatase crystal phase or the higher temperature rutile phase in aggregate. As one of the most heavily studied metal oxide materials for photoelectrochemistry, the optical properties of TiO_2 nanoparticles and films doped with Er have also been investigated for applications in photocatalysis and photodetection, where high concentrations ($\lesssim 1$ at%) of Er act as up-conversion sensitizers in the visible range.^{20–22}

In the anatase phase, the optical transition between the lowest crystal field-split levels in the ground and first excited states (Z_1 - Y_1) emits at a wavelength near 1533 nm.^{19,23} Meanwhile, in the rutile phase, the Z_1 - Y_1 transition is near 1520 nm.¹⁵ This considerable difference in the transition energies between the two phases yields opportunities for spectrally isolating quantum emitters of interest. In parallel, prior efforts have demonstrated the ability to locally adjust the crystalline phase of TiO_2 films and nanoparticles by laser annealing, showing conversion from amorphous films to a crystalline phase or from anatase to rutile as detected by micro-Raman spectroscopy^{24–26} or transmission electron microscopy.²⁷ As with other solid-state quantum emitters, such as those based on crystalline defects, a key challenge for scalable quantum technologies is the deterministic spatial placement of the emitter within a desired crystal volume. Laser writing has been used as a localization technique for generating vacancy complex-based quantum emitters in diamond²⁸ and silicon carbide.²⁹ In a similar vein, we utilize micro-focused laser annealing as a means toward localization of Er^{3+} emitters in TiO_2 thin films. Here, we demonstrate localized anatase to rutile conversion of moderately Er-doped TiO_2 films with near diffraction-limited spatial resolution. We use cryogenic photoluminescence mapping and nanoprobe synchrotron-based X-ray diffraction measurements to confirm the phase transition and to measure rutile grain size.

II. MAIN

Polycrystalline thin films of TiO_2 were grown on silicon substrates in a molecular beam deposition chamber. The growth method and phase control via growth temperature are described in more detail elsewhere.¹⁷ In this work, all measurements were performed on a 55 nm-thick polycrystalline anatase film grown on 3-inch Si(100), which comprised three layers (40 nm, 10 nm, and 5 nm from bottom to top) with the middle 10 nm doped with erbium at a ~ 500 parts per million (ppm) concentration (Fig. 1(a) inset). This wafer was subsequently diced into chips for different annealing experiments. The particular film stack was chosen to maximize the observed brightness of the Er^{3+} photoluminescence in this experiment while maintaining a thin profile with an eye toward integrated quantum photonic applications.¹⁸

The films were loaded into an optical cryostat integrated with a custom confocal microscope setup as shown in Fig. 1(a). During the laser annealing process, the films

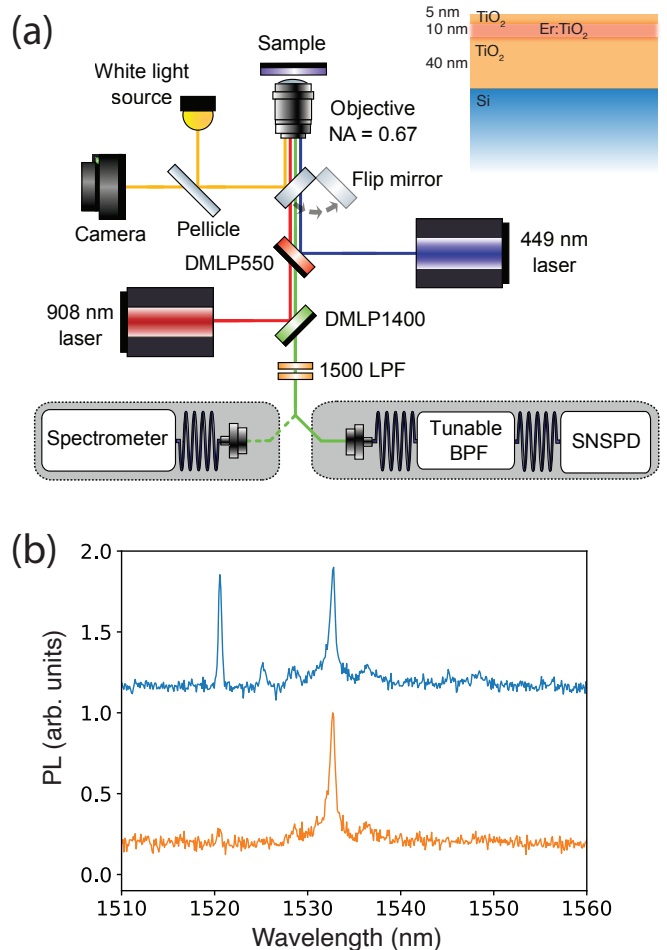


FIG. 1. (a) A simplified schematic of the experimental setup (DMLP: dichroic mirror long pass, LPF: long pass filter, BPF: band pass filter, SNSPD: superconducting nanowire single-photon detector). A blue laser ($\lambda = 449$ nm) is used for the laser anneal of the Er-doped TiO_2 films. An off-resonant laser ($\lambda = 908$ nm) is used for the optical excitation for the cryogenic photoluminescence measurements. The Er emission collected by the objective passes through dichroic mirrors and filters and is detected by the spectrometer or the SNSPD. The inset shows a schematic of the Er-doped TiO_2 film stack. (b) Representative photoluminescence spectra of Er: TiO_2 before laser annealing (orange) and after annealing (blue). Measurements taken at $T=3.6$ K.

were kept at room temperature and under ambient atmospheric conditions while a variable power $\lambda = 449$ nm continuous wave (CW) laser was tightly focused through an air objective lens with an N.A. of 0.67. The objective lens was mounted on a three-dimensional periscope stage, which allowed the control of the position and focus of the laser beam with respect to the sample films. The laser anneal was performed in sets of arrays of 12 spots with 5 μm spacings, wherein among the different sets, the effective $\lambda = 449$ nm laser power was varied from below 100 mW to approximately 185 mW (at sample position) and

the duration of the laser anneal was varied from 1 to 100 seconds. After the laser annealing step, the films were quickly evaluated for phase change as-is, or they underwent a post-laser-annealing process in a tube furnace in a 20% O₂/balance N₂ environment heated to either 400 °C or 500 °C for one hour. A quick verification of phase change could be confirmed by measuring the photoluminescence (PL) spectra of the films (Fig. 1(b)).

We observe that laser annealing at high powers causes a morphological change in the films. Figure 2(a) shows a scanning electron micrograph of a laser-annealed spot (1 second, 185 mW) after a 400°C post-anneal. We see that for these conditions, the visibly small grains of the surrounding polycrystalline film undergo grain growth within the irradiated spot, which is on the order of 450 nm in diameter and is only slightly larger than the expected diffraction-limited $1/e$ Gaussian beam diameter of $0.62\lambda/\text{NA} \approx 415$ nm for an overfilled objective lens.

To investigate local changes in the crystal phase, we performed scanning X-ray diffraction microscopy measurements on the Hard X-ray Nanoprobe Beamline operated by the Center for Nanoscale Materials at the Advanced Photon Source at Argonne National Laboratory. A 10 keV X-ray beam was focused to a 20 nm spot and scanned across the surface of a laser-annealed film. In contrast to the chips with the arrays of 12 identical laser annealed spots, this chip was diced from the same wafer and patterned with Cr fiducial markers. Subsequent laser annealing was performed in an array between the markers, varying the laser power in each row and increasing the laser annealing time in each column of the array. This chip was then annealed for 1 hour at 400°C in 20% O₂ prior to the XRD measurements. As shown in Fig. 2, rutile X-ray diffraction was only observed for the highest laser annealing power (185 mW) used in this array. Figure 2(b) shows the summed diffraction pattern from a raster scan covering an area of $3 \times 3 \mu\text{m}^2$. The anatase 101 reflection exhibits a continuous powder ring due to the random crystal orientation of the nanosized crystalline grains within the probed region. A donut-shaped diffraction spot was observed at the 2θ value for the rutile 110 reflection. The donut is an image of the focusing optics, the appearance of which indicates good crystallinity. We note that the crystal orientation of the rutile phase is also random, but the diffraction spots of the rutile phase do not form a continuous ring because statistically only the diffraction from one or two grains can be observed on the detector for a given incident angle. Diffraction from other rutile grains were observed after tilting the sample to different incident angles. Figure 2(c) shows a dark field image of 29 rutile grains observed for an incident angle range of 6.0° to 12.8° . The rutile phase was only found at a few locations scattered between the two Cr fiducial markers. These locations are consistent with the position of the laser annealed spots at a power of 185 mW. In this particular laser-annealed sample, the next lowest laser power used was < 100 mW and no rutile signal was observed. The size of individual rutile grains

was determined by performing refined line scans across individual grains and fitting the rutile diffraction signal with a Gaussian profile. The average size of the 29 grains is about 88 nm as shown in Fig. 2(d).

We additionally investigated the effect of laser annealing power and duration on the Er:rutile transition through cryogenic PL measurements. After the laser annealing and a subsequent tube furnace annealing process, the films were cooled to $T=3.6$ K and excited with an off-resonant $\lambda = 908$ nm laser. The PL spectra collected from the laser annealed areas showed an enhanced PL signal at about 1520 nm along with the peak at about 1533 nm, attributed to Er:rutile and Er:anatase, respectively (Fig. 1(b)). The rutile PL signal was selectively collected using a tunable bandpass filter set to a center wavelength of 1520 nm and a FWHM of 950 pm positioned before the superconducting nanowire single photon detector (SNSPD). As the excitation laser was scanned across the sample, clear and bright micron-scale spots were observed as in Fig. 3(a). We note that laser annealing powers below about 169 mW incident on the sample with 1 second duration yielded no detectable phase change while a weak rutile signal appeared when increasing the duration to 10 seconds. As shown in Fig. 3(c), post-annealing at 500 °C seemed to have a similar effect on the PL scans compared to 400 °C. While the post-anneal in the tube furnace was not critical to observe the anatase→rutile transition, we ultimately found that the intensity of the principle rutile PL line was dramatically increased after the furnace annealing. We additionally attempted laser annealing with the same conditions in a partial vacuum environment (few mTorr) at room temperature and at 3.6 K; however, no rutile PL signal was observed. This is in contrast to a prior work, which observed anatase→rutile transition in thin films after annealing in vacuum with high-power 532 nm excitation focused to a spot size of about $100 \mu\text{m}$.²⁶ Meanwhile, the presence of oxygen vacancies and their enhanced ionic mobility in the presence of an oxygen-rich atmosphere has been proposed as a mechanism by which the anatase→rutile transition can occur during photoexcitation at below-gap energies (< 3.2 eV).²⁵ We attribute the apparent lack of phase conversion to the reduced oxygen concentration during the laser annealing process. This further suggests a phase change mechanism that is not based on heating alone from the below-gap excitation.

Next, we remove the tunable bandpass filter and directly collect the PL signal with a spectrometer at the locations that showed the bright spots in the rutile-filtered spatial maps. Fitting each of these peaks to Lorentzian profiles, we examine the rutile/anatase integrated intensity ratio—in order to account for any drifts in focus—as the annealing laser power is increased. Figures 3(b) and (d) show the intensity ratio I_R/I_A for films that underwent 400 °C and 500 °C post-anneals, respectively, while the blue circles correspond to 1 second laser anneals and the red squares correspond to 10 second laser anneals. We find that the intensity ratio increases lin-

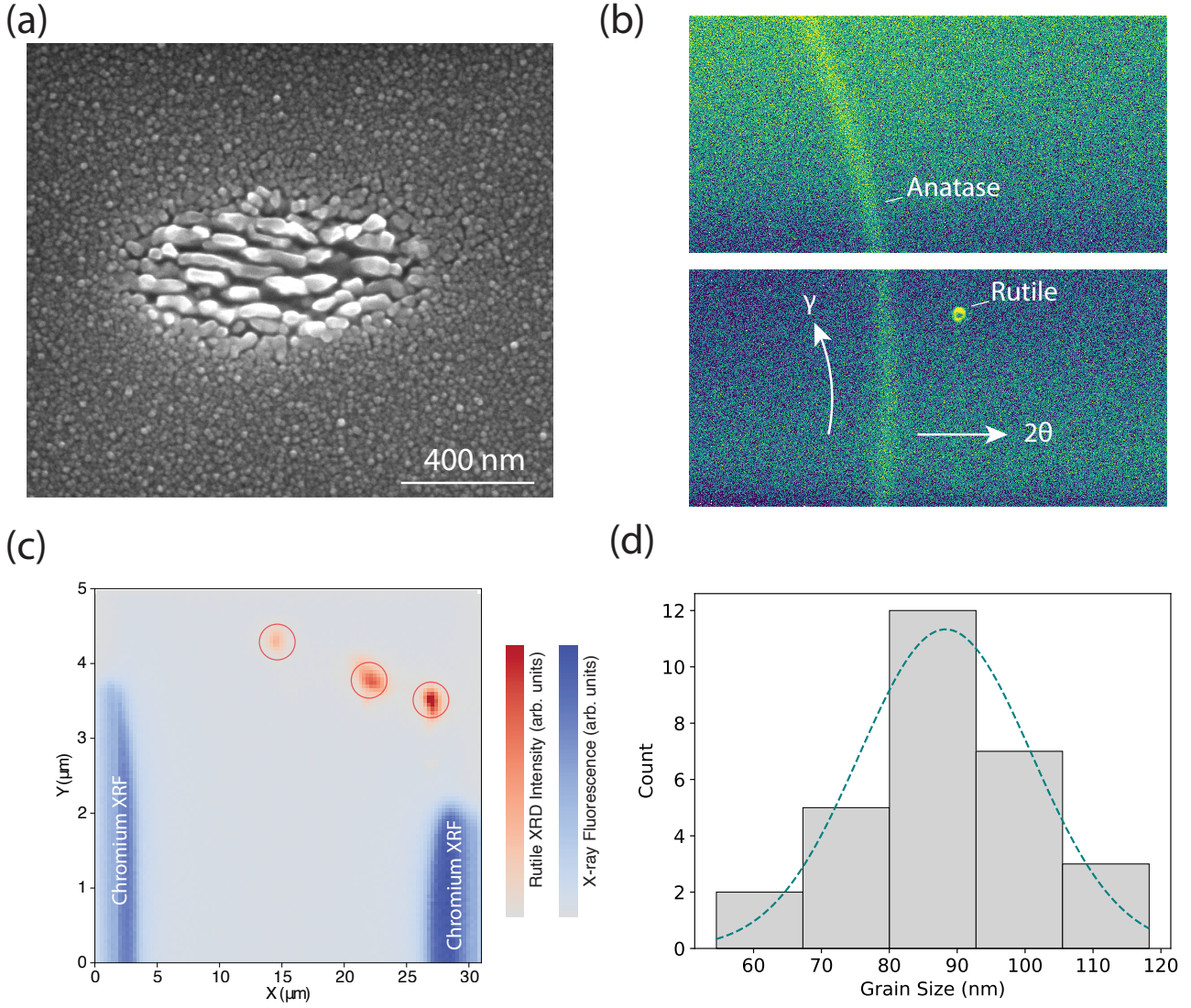


FIG. 2. (a) Scanning electron micrograph of a single laser-annealed spot on an anatase film (1 second at ~ 185 mW, post-anneal 400°C for 1 hour in 20% O_2) showing grain growth in the center. (b) X-ray diffraction pattern produced by summing up all the detector images acquired during a $3 \times 3 \mu\text{m}^2$ raster scan on a film patterned with Cr alignment markers. The angular 2θ range covers both the anatase 101 and the rutile 110 reflections. The continuous ring along the γ direction is formed by diffraction from crystals with random orientations. (c) Composite image showing the locations of the rutile phase. The real-space image was produced by summing up dark field images of the rutile 110 reflection acquired over a range of incidence angles between 6.0 and 12.8° . The spots are wider in the X direction due to the projection of the incident X-ray beam at shallow incident angles. Red circles highlight three laser-exposed spots (~ 185 mW, 1 sec, 10 sec, 100 sec left to right). Also shown is X-ray fluorescence signal from the nearby Cr alignment structures. (d) Statistics of measured individual rutile grains extracted from spatial scans. The teal dashed line is a Gaussian fit to the data, indicating an average grain size of 88 ± 30 nm.

early with laser power; however, for the 169 mW annealing case, phase conversion was only observed for exposure times ≥ 10 seconds. Additionally, as the post-anneal temperature increases, we observe an increase in the relative anatase intensity and a decrease in the intensity of the background PL signal. This increase in anatase signal with increasing post-anneal temperature could be potentially attributed to further crystallization and grain growth of nearby anatase grains while staying

below the point of the rutile transition. It should be additionally noted that the diffraction-limited probe laser spot (at $\lambda = 908$ nm) used for PL measurements would be considerably larger than the $\lambda = 449$ nm annealing laser. Thus, the PL signal will include anatase phase TiO_2 from the periphery of the annealed spot. The decrease in the background intensity, meanwhile, is likely attributable to healing of other crystalline defects and desorption/combustion of carbon compounds on the sur-

face that may contribute to fluorescence.

Lastly, we demonstrate laser-induced anatase→rutile phase change on microstructures etched into the Si substrate. We first patterned ridge-like structures into the Si through standard photolithography and plasma etching. These structures range from approximately 500 nm to a couple of microns in width and are approximately 3 μm tall (Fig. 4(a)). After fabrication, we laser annealed the TiO_2 films on top of the ridges; however, instead of spot annealing, we scanned the laser across the ridges at a rate of 5 mm/sec. For each vertical cross-cut, we set a different laser power. After a 400 °C post-anneal, rutile PL is visible at low temperatures for regions exposed to the three highest annealing powers, as shown in Fig. 4(b). Examining these annealed spots under SEM, we observe similar morphological changes in the TiO_2 films, often concentrated near the edges of ridge (Fig. 4(c-d)). Additionally, we observe occasional straggle along the direction of the ridge, which is transverse to the direction of laser scanning. We attribute this straggle to vibrations in the assembly holding the objective lens. Future improvements to the laser scanning assembly design can mitigate unwanted vibrations or straggle of the focused laser spot, which could, for example, ultimately facilitate the placement of Er:rutile at the anti-node of a photonic crystal cavity. Beyond the anatase→rutile transition, sub-bandgap laser annealing has been shown to crystallize amorphous TiO_2 films,²⁵ as well as to effectively transform rutile back to anatase through amorphization of the rutile phase and subsequent anatase crystallization.²⁶ Fully reversible phase control would provide an important tuning knob, especially when considering Er: TiO_2 films that are evanescently coupled to proximal photonic cavities whose resonant wavelength is deeply affected by the local environment.

III. CONCLUSION

In conclusion, we have demonstrated local, submicron anatase→rutile phase conversion of Er: TiO_2 thin films grown on Si using below-gap ($\lambda = 449$ nm) laser excitation. This phase change was found to occur most readily when the laser annealing was performed in standard atmosphere and at room temperature, and the Er^{3+} photoluminescence, especially that of the anatase phase, was improved by post-annealing in an oxygen-rich environment. While the rutile PL signal increased linearly with laser power, no phase change was observed by PL for annealing powers below about 169 mW, except for longer duration anneals (10 seconds). In addition, nanoscale X-ray diffraction measurements highlight the improved crystallinity of the rutile grains, vis-à-vis anatase, attributed to the laser annealing. Fine spatial scans indicated an average grain size of 88 ± 30 nm. Finally, we demonstrated that this same phase change process can be extended to TiO_2 films on Si microstructures, which are similar in form to waveguide structures in Si photonics.

Through further tuning of the anneal parameters and improvements in the laser positioning capabilities, the ability to adjust the phase of host materials with submicron resolution coupled with delta doping, opens up a new avenue for deterministic placement of quantum emitters and spin qubits.

ACKNOWLEDGMENTS

The authors thank Nazar Deegan and Robert Pettit for helpful discussions. Work at Argonne (M.V.H., D.D.A., S.G., F. J. H.) was supported by the U.S. Department of Energy, Office of Science, National Quantum Information Science Research Centers as part of Q-NEXT. We acknowledge additional support from the U.S. Department of Energy, Office of Basic Energy Sciences, Materials Science and Engineering Division (J.A.). Work by S.E.S. and M.K.S. was carried out at Argonne National Laboratory with support from the U.S. Department of Energy Office of Science Advanced Scientific Computing Research program under CRADA A22112 through the Chain Reaction Innovations program. Work performed at the Center for Nanoscale Materials and Advanced Photon Source, both U.S. Department of Energy Office of Science User Facilities, was supported by the U.S. DOE, Office of Basic Energy Sciences, under Contract No. DE-AC02-06CH11357.

- ¹G. Wolfowicz, F. J. Heremans, C. P. Anderson, S. Kanai, H. Seo, A. Gali, G. Galli, and D. D. Awschalom, “Quantum guidelines for solid-state spin defects,” *Nature Reviews Materials* **6**, 906–925 (2021), number: 10 Publisher: Nature Publishing Group.
- ²T. Boettger, Y. Sun, C. W. Thiel, and R. L. Cone, “Material optimization of $\text{Er}^{3+}:\text{Y}_2\text{SiO}_5$ at 1.5 μm for optical processing, memory, and laser frequency stabilization applications,” in *Advanced Optical Data Storage*, Vol. 4988 (SPIE, 2003) pp. 51–61.
- ³M. Rani, M. P. Hedges, R. L. Ahlefeldt, and M. J. Sellars, “Coherence time of over a second in a telecom-compatible quantum memory storage material,” *Nature Physics* **14**, 50–54 (2018), number: 1 Publisher: Nature Publishing Group.
- ⁴M. Le Dantec, M. Rani, S. Lin, E. Billaud, V. Ranjan, D. Flanigan, S. Bertaina, T. Chanelire, P. Goldner, A. Erb, R. B. Liu, D. Esteve, D. Vion, E. Flurin, and P. Bertet, “Twenty-threemillisecond electron spin coherence of erbium ions in a natural-abundance crystal,” *Science Advances* **7**, eabj9786 (2021), publisher: American Association for the Advancement of Science.
- ⁵S. Gupta, X. Wu, H. Zhang, J. Yang, and T. Zhong, “Robust Millisecond Coherence Times of Erbium Electron Spins,” *Physical Review Applied* **19**, 044029 (2023), publisher: American Physical Society.
- ⁶R. M. Pettit, F. H. Farshi, S. E. Sullivan, V. Vliz-Osorio, and M. K. Singh, “A perspective on the pathway to a scalable quantum internet using rare-earth ions,” (2023), arXiv:2304.07272 [quant-ph].
- ⁷A. Dibos, M. Raha, C. Phenicie, and J. Thompson, “Atomic Source of Single Photons in the Telecom Band,” *Physical Review Letters* **120**, 243601 (2018), publisher: American Physical Society.
- ⁸S. Ourari, L. Dusanowski, S. P. Horvath, M. T. Uysal, C. M. Phenicie, P. Stevenson, M. Raha, S. Chen, R. J. Cava, N. P. de Leon, and J. D. Thompson, “Indistinguishable telecom band photons from a single erbium ion in the solid state,” (2023), arXiv:2301.03564 [physics, physics:quant-ph].

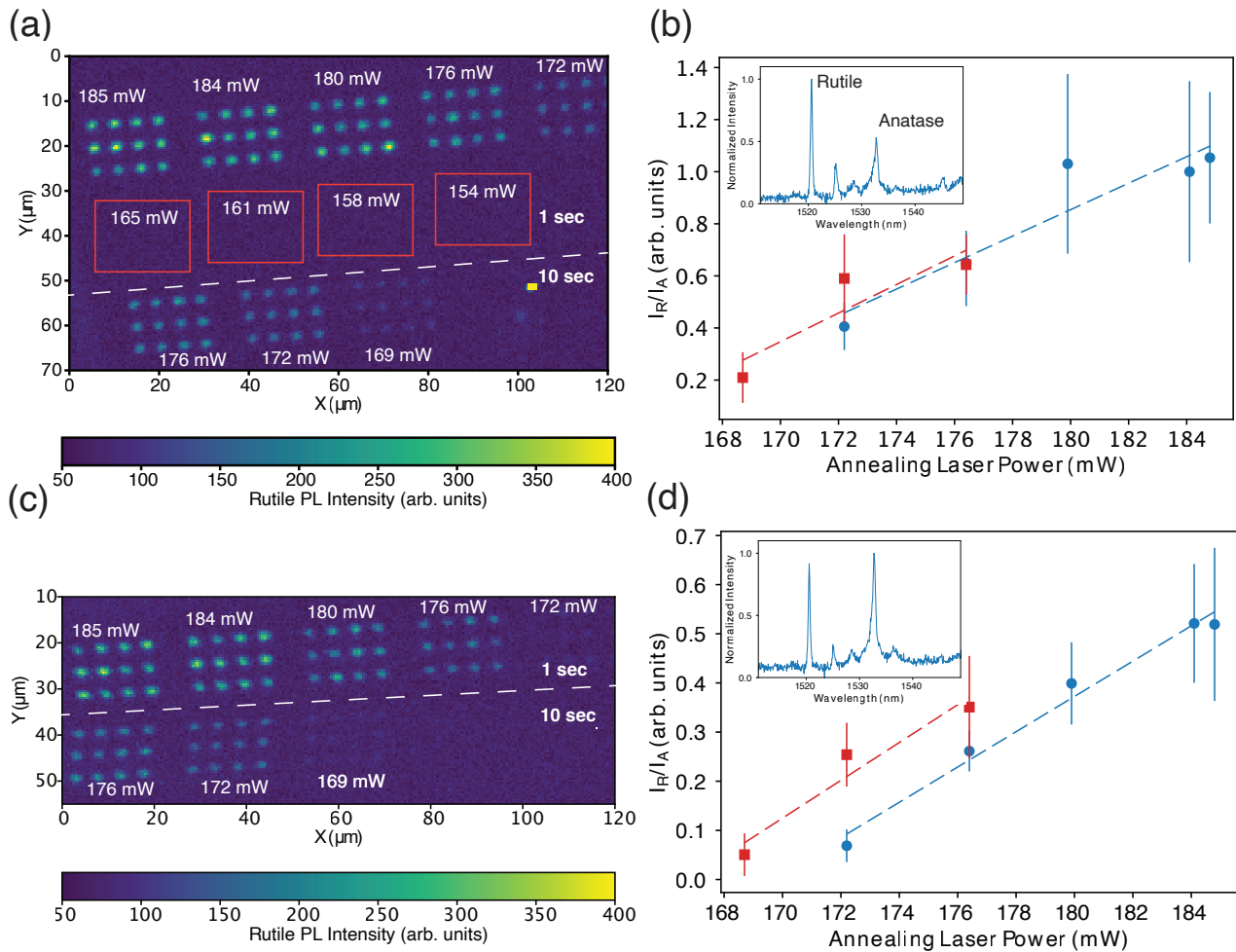


FIG. 3. (a) Spatial map of the laser annealing dose array showing rutile-filtered PL. Blocks of 12 points share identical laser annealing conditions, as indicated by the labels. Regions that were annealed at lower powers that did not result in visible phase change are indicated by red boxes. (b) Rutile/anatase integrated intensity ratio as a function of laser annealing power. The points represent the average measured value for the 12 annealed spots in each array block in (a). Blue circles correspond to 1 second laser annealing times and red squares represent 10 second laser anneals. The dashed lines are linear fits to the measurement data. The inset shows the averaged spectrum for 1 second laser anneals at the maximum laser power in each case. Error bars are calculated from the standard deviation of the 12 measurements for each condition at the 95% confidence level. Both (a) and (b) show results for the $T=400$ °C post-annealed film. (c) The PL map and (d) integrated rutile/anatase intensity ratio for the $T=500$ °C post-annealed film. The bright spot visible in (a) is an artifact from a scratch on the film surface.

- ⁹M. Raha, S. Chen, C. M. Phenicie, S. Ourari, A. M. Dibos, and J. D. Thompson, “Optical quantum nondemolition measurement of a single rare earth ion qubit,” *Nature Communications* **11**, 1605 (2020), number: 1 Publisher: Nature Publishing Group.
- ¹⁰S. Chen, M. Raha, C. M. Phenicie, S. Ourari, and J. D. Thompson, “Parallel single-shot measurement and coherent control of solid-state spins below the diffraction limit,” *Science* **370**, 592–595 (2020), publisher: American Association for the Advancement of Science.
- ¹¹A. Ortu, A. Tiranov, S. Welinski, F. Frwis, N. Gisin, A. Ferrier, P. Goldner, and M. Afzelius, “Simultaneous coherence enhancement of optical and microwave transitions in solid-state electronic spins,” *Nature Materials* **17**, 671–675 (2018), number: 8 Publisher: Nature Publishing Group.

- ¹²P. Stevenson, C. M. Phenicie, I. Gray, S. P. Horvath, S. Welinski, A. M. Ferrenti, A. Ferrier, P. Goldner, S. Das, R. Ramesh, R. J. Cava, N. P. de Leon, and J. D. Thompson, “Erbium-implanted materials for quantum communication applications,” *Physical Review B* **105**, 224106 (2022), publisher: American Physical Society.
- ¹³A. M. Ferrenti, N. P. de Leon, J. D. Thompson, and R. J. Cava, “Identifying candidate hosts for quantum defects via data mining,” *npj Computational Materials* **6**, 1–6 (2020), number: 1 Publisher: Nature Publishing Group.
- ¹⁴S. Kanai, F. J. Heremans, H. Seo, G. Wolfowicz, C. P. Anderson, S. E. Sullivan, M. Onizhuk, G. Galli, D. D. Awschalom, and H. Ohno, “Generalized scaling of spin qubit coherence in over 12,000 host materials,” *Proceedings of the National Academy of Sciences* **119**, e2121808119 (2022), publisher: Proceedings of the

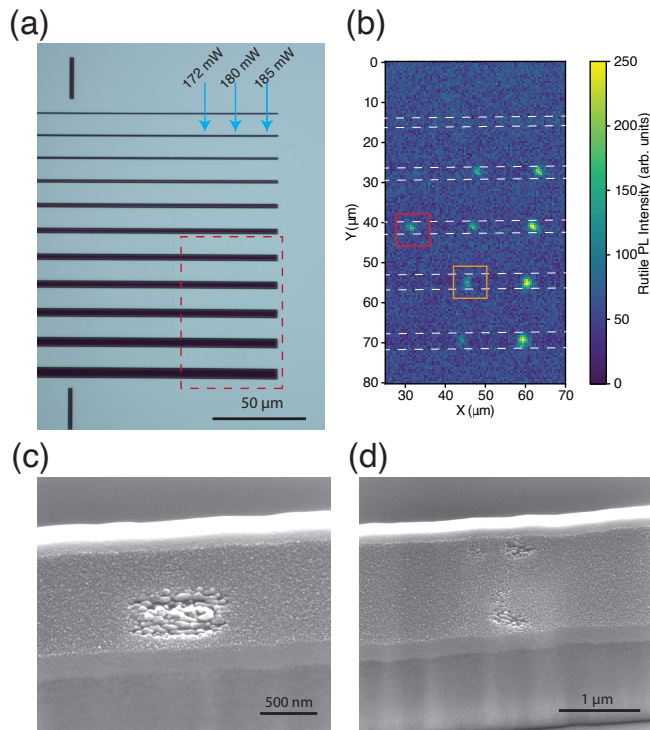


FIG. 4. (a) An optical micrograph of the etched ridge structures, depicting the path of the laser at the three highest powers (blue arrows). (b) The PL map corresponding to the red outlined rectangle in (a) with white dashed lines highlighting the ridge structures for clarity. (c) and (d) Scanning electron micrographs of the annealing conditions highlighted in (b) by red and orange squares, respectively.

- National Academy of Sciences.
- ¹⁵C. M. Phenicie, P. Stevenson, S. Welinski, B. C. Rose, A. T. Asfaw, R. J. Cava, S. A. Lyon, N. P. de Leon, and J. D. Thompson, "Narrow Optical Line Widths in Erbium Implanted in TiO₂," *Nano Letters* **19**, 8928–8933 (2019), publisher: American Chemical Society.
- ¹⁶S. S. Djordjevic, K. Shang, B. Guan, S. T. S. Cheung, L. Liao, J. Basak, H.-F. Liu, and S. J. B. Yoo, "CMOS-compatible, athermal silicon ring modulators clad with titanium dioxide," *Optics Express* **21**, 13958–13968 (2013), publisher: Optica Publishing Group.
- ¹⁷M. K. Singh, G. Wolfowicz, J. Wen, S. E. Sullivan, A. Prakash, A. M. Dibos, D. D. Awschalom, F. J. Heremans, and S. Guha, "Development of a Scalable Quantum Memory Platform – Materials Science of Erbium-Doped TiO₂ Thin Films on Silicon," (2022), arXiv:2202.05376 [cond-mat, physics:physics].

- ¹⁸A. M. Dibos, M. T. Solomon, S. E. Sullivan, M. K. Singh, K. E. Sautter, C. P. Horn, G. D. Grant, Y. Lin, J. Wen, F. J. Heremans, S. Guha, and D. D. Awschalom, "Purcell Enhancement of Erbium Ions in TiO₂ on Silicon Nanocavities," *Nano Letters* **22**, 6530–6536 (2022), publisher: American Chemical Society.
- ¹⁹K. Shin, I. Gray, G. Marcaud, S. P. Horvath, F. J. Walker, J. D. Thompson, and C. H. Ahn, "Er-doped anatase TiO₂ thin films on LaAlO₃ (001) for quantum interconnects (QuICs)," *Applied Physics Letters* **121**, 081902 (2022).
- ²⁰S. Mondal, A. Ghosh, M. R. Piton, J. P. Gomes, J. F. Felix, Y. G. Gobato, H. V. A. Galeti, B. Choudhuri, S. M. M. Dhar Dwivedi, M. Henini, and A. Mondal, "Investigation of optical and electrical properties of erbium-doped TiO₂ thin films for photodetector applications," *Journal of Materials Science: Materials in Electronics* **29**, 19588–19600 (2018).
- ²¹Z. Rao, X. Xie, X. Wang, A. Mahmood, S. Tong, M. Ge, and J. Sun, "Defect Chemistry of Er³⁺-Doped TiO₂ and Its Photocatalytic Activity for the Degradation of Flowing Gas-Phase VOCs," *The Journal of Physical Chemistry C* **123**, 12321–12334 (2019), publisher: American Chemical Society.
- ²²A. Kot, M. Radecka, and K. Zakrzewska, "Influence of Er and Yb on photoelectrochemical performance of TiO₂ thin film," *Applied Surface Science* **608**, 155127 (2023).
- ²³S. R. Johannsen, S. Roesgaard, B. Julsgaard, R. a. S. Ferreira, J. Chevallier, P. Balling, S. K. Ram, and A. N. Larsen, "Influence of TiO₂ host crystallinity on Er³⁺ light emission," *Optical Materials Express* **6**, 1664–1678 (2016), publisher: Optica Publishing Group.
- ²⁴G. C. Vsquez, M. A. Peche-Herrero, D. Maestre, A. Gianoncelli, J. Ramirez-Castellanos, A. Cremades, J. M. Gonzalez-Calbet, and J. Piqueras, "Laser-Induced Anatase-to-Rutile Transition in TiO₂ Nanoparticles: Promotion and Inhibition Effects by Fe and Al Doping and Achievement of Micropatterning," *The Journal of Physical Chemistry C* **119**, 11965–11974 (2015), publisher: American Chemical Society.
- ²⁵J. A. Benavides, C. P. Trudeau, L. F. Gerlein, and S. G. Cloutier, "Laser Selective Photoactivation of Amorphous TiO₂ Films to Anatase and/or Rutile Crystalline Phases," *ACS Applied Energy Materials* **1**, 3607–3613 (2018), publisher: American Chemical Society.
- ²⁶S. E. Ahmed, V. M. Poole, J. Igo, Y. Gu, and M. D. McCluskey, "Localized phase transition of TiO₂ thin films induced by sub-bandgap laser irradiation," *Journal of Vacuum Science & Technology A* **39**, 053402 (2021).
- ²⁷M. Abbasi, Y. Dong, J. Meng, D. Morgan, X. Wang, and J. Hwang, "In situ observation of medium range ordering and crystallization of amorphous TiO₂ ultrathin films grown by atomic layer deposition," *APL Materials* **11**, 011102 (2023).
- ²⁸Y.-C. Chen, B. Griffiths, L. Weng, S. S. Nicley, S. N. Ishmael, Y. Lekhai, S. Johnson, C. J. Stephen, B. L. Green, G. W. Morley, M. E. Newton, M. J. Booth, P. S. Salter, and J. M. Smith, "Laser writing of individual nitrogen-vacancy defects in diamond with near-unity yield," *Optica* **6**, 662 (2019).
- ²⁹Y.-C. Chen, P. S. Salter, M. Niethammer, M. Widmann, F. Kaiser, R. Nagy, N. Morioka, C. Babin, J. Erlekampf, P. Berwian, M. J. Booth, and J. Wrachtrup, "Laser Writing of Scalable Single Color Centers in Silicon Carbide," *Nano Letters* **19**, 2377–2383 (2019), publisher: American Chemical Society.